



Sawtooth patterns in flexural force curves of structural biological materials are not signatures of toughness enhancement: Part I

Sayaka Kochiyama, Wenqiang Fang, Michael A. Monn, Haneesh Kesari*

184 Hope Street, Providence, RI, 02912, USA



ARTICLE INFO

Keywords:

Structure-property relationship
Experimental mechanics
Damage tolerance
Architectured materials

ABSTRACT

Layered architectures are prevalent in tough biological composites, such as nacre and bone. Another example of a biological composite with layered architecture is the skeletal elements—called spicules—from the sponge *Euplectella aspergillum*. Based on the similarities between the architectures, it has been speculated that the spicules are also tough. Such speculation is in part supported by a sequence of sudden force drops (sawtooth patterns) that are observed in the spicules' force-displacement curves from flexural tests, which are thought to reflect the operation of fracture toughness enhancing mechanisms. In this study, we performed three-point bending tests on the spicules, which also yielded the aforementioned sawtooth patterns. However, based on the analysis of the micrographs obtained during the tests, we found that the sawtooth patterns were in fact a consequence of slip events in the flexural tests. This is put into perspective by our recent study, in which we showed that the spicules' layered architecture contributes minimally to their toughness, and that the toughness enhancement in them is meager in comparison to what is observed in bone and nacre [Monn MA, Vijaykumar K, Kochiyama S, Kesari H (2020): *Nat Commun* 11:373]. Our past and current results underline the importance of inferring a material's fracture toughness through direct measurements, rather than relying on visual similarities in architectures or force-displacement curve patterns. Our results also suggest that since the spicules do not possess remarkable toughness, re-examining the mechanical function of the spicule's intricate architecture could lead to the discovery of new engineering design principles.

1. Introduction

Fracture toughness, in general, describes the material's ability to resist propagation of a pre-existing crack. Preventing catastrophic failure that occurs through the propagation of brittle cracks is critical for ensuring integrity and safety in engineering applications. As such, fracture toughness is regarded as one of the key criteria in the selection of structural materials. Consequently, the materials development community is always interested in new methodologies for increasing the fracture toughness of engineering materials.

Some stiff biological materials (SBMs) are well known for being natural ceramic composites whose fracture toughness far exceeds what is expected by the simple rule of mixtures (Wegst et al., 2014). For this reason, SBMs serve as an attractive model material class in studies aimed at improving the fracture toughness of synthetic composites. Shells and bone are prototypical examples of SBMs that demonstrate and are

studied for their enhanced fracture toughness (see Fig. 1). For instance, nacre—the iridescent part of some mollusk shells—demonstrates a 1000-fold increase in fracture toughness¹ compared to that of the mineral aragonite, which constitutes over 95% of the shell by volume (Currey, 1977; Jackson et al., 1988).

The enhanced fracture toughness in prototypically tough SBMs is known to be a direct consequence of their intricate internal architectures (Barthelat and Rabiei, 2011; Rabiei et al., 2012; Jackson et al., 1988; Browning et al., 2013; Munch et al., 2008; Kolednik et al., 2011; Zlotnikov et al., 2013; Clegg et al., 1990). These internal architectures are also referred to as layered architectures since they often consist of alternating stiff ceramic layers and compliant organic layers that are laid out in intricate three-dimensional (3D) patterns. The precise mechanisms of how the internal architectures contribute to enhanced fracture toughness is of particular interest to the materials engineering community, since such an understanding would be more flexible and

Abbreviations: SBMs, stiff biological materials; SS, simply-supported; FF, fixed-fixed; MTS, mechanical testing stage.

* Corresponding author.

E-mail address: haneesh_kesari@brown.edu (H. Kesari).

¹ This enhancement is in terms of work of fracture

<https://doi.org/10.1016/j.jmbbm.2021.104362>

Received 21 October 2020; Received in revised form 3 January 2021; Accepted 22 January 2021

Available online 5 March 2021

1751-6161/© 2021 Elsevier Ltd. All rights reserved.

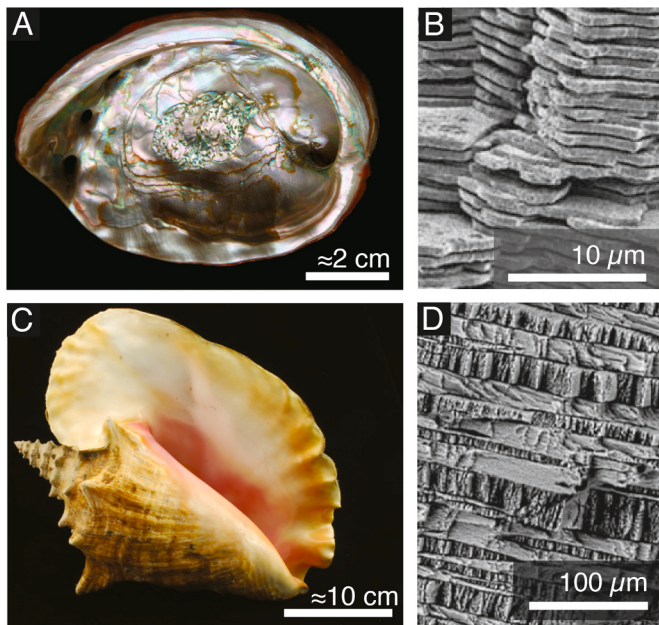


Fig. 1. Examples of layered architectures in biological materials. (A) The shell of *Haliotis rufescens*—the red abalone (image courtesy of John Varner). (B) A scanning electron microscope (SEM) image of nacre from *H. rufescens* showing its brick-and-mortar layered architecture, where aragonite tablets are the bricks and protein layers function as the mortar (modified with permission from (Rabiei et al., 2012); copyright 2012 Royal Society of Chemistry). (C) The shell of *Strombus gigas*—the queen conch (image courtesy of John Varner). (D) The layered architecture of the *S. gigas* shell (modified with permission from (Osuna-Mascaró et al., 2014); copyright 2014 Elsevier).

effective for designing bioinspired composites than directly copying all aspects of the architecture.

Several mechanisms have been put forward for explaining how the SBMs' layered architectures enhance their fracture toughness (Barthelat et al., 2007; Smith et al., 1999; Jackson et al., 1988; Meyers et al., 2008; Li et al., 2004; Kamat et al., 2004). One of the most popular is the Cook-Gordon mechanism (Cook et al., 1964), whose details are provided in Fig. 2. A consequence of the operation of the Cook-Gordon mechanism is the occurrence of a sequence of sudden force drops in the force-displacement (or equivalently stress-strain) curves obtained from flexural tests that terminates when the specimen fails completely. Following Sarikaya et al. (2001), we refer to such sequences as “sawtooth patterns”. As shown in Fig. 2, the beginning of a force drop corresponds to the re-initiation of an arrested crack through the sprouting of a new branch, and the end of that force drop corresponds to the re-arrest of the crack via deflection/trapping of the new branch at the next weak interface. Thus, a sawtooth pattern is a reflection of several layer-fracture events that occur one after another on the force-displacement curve.

In recent decades, some skeletal structures from marine sponges are attracting increased attention as potential new additions to the list of prototypically tough SBMs. These skeletal structures, which are known as spicules,² are fiber or rod-like composite structures that are predominantly composed of biogenic silica and have a layered architecture. As a representative example, in Fig. 3 we show the spicules from the marine sponge *Euplectella aspergillum* (*Ea.*) and their layered

architecture. These spicules function as anchors to keep the *Ea.* sponge fixed onto the sea floor (Weaver et al., 2010), and are also called basalia spicules or anchor spicules for their function. For the sake of simplicity, we will refer to them as *Ea.* spicules or just as spicules when it is clear from context. Spicules are being considered as one of the latest additions to the list of prototypically tough SBMs primarily because the spicules' layered architecture has a striking resemblance to the ones seen in prototypically tough SBMs (compare, e.g., Fig. 1(B), (D) with Figs. 3(C) and 4(B), (D)).

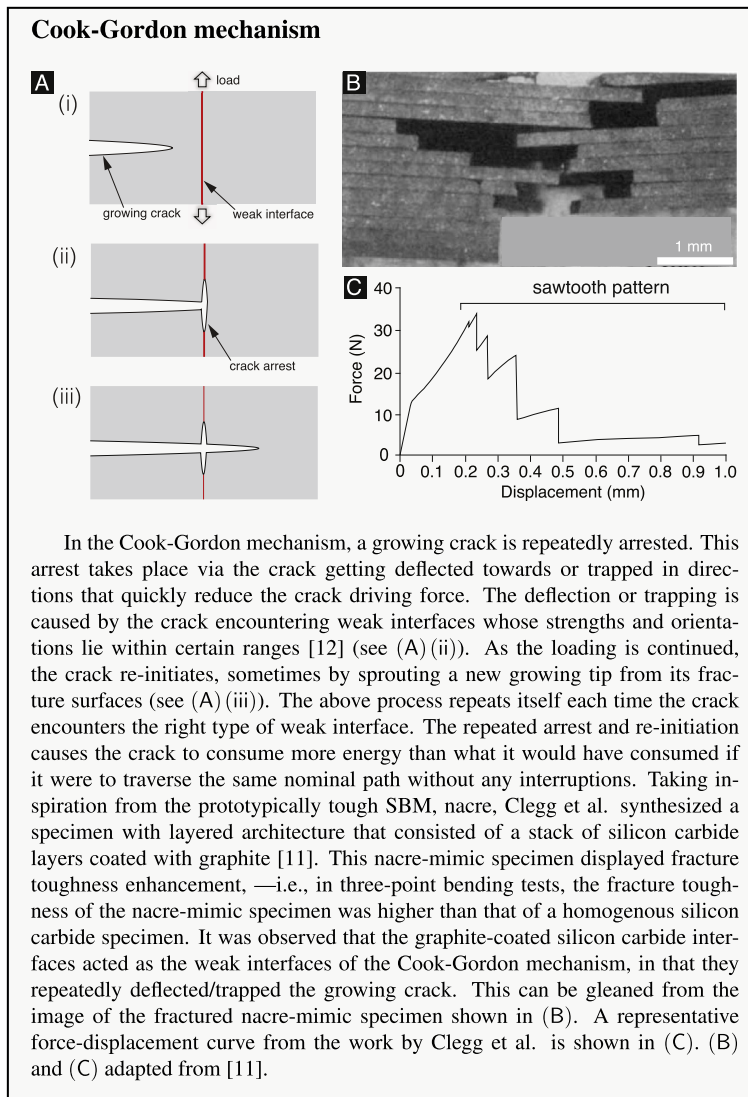
It is prudent, however, to first thoroughly establish that the fracture toughness is indeed enhanced in the spicules instead of relying solely on the visual similarities of their internal architectures with those of prototypically tough SBMs. This is because once it becomes accepted that the fracture toughness of a biological material benefits from its internal architecture, significant resources get expended in unraveling the details of the underlying fracture toughness enhancing mechanisms as well as in mimicking the internal architecture in synthetic composites. In this paper, we focus on the question of fracture toughness enhancement in spicules and, following Monn et al. (2020), argue that at least in the case of *Ea.* spicules, there is no substantial fracture toughness enhancement. The implication of our arguments for bioinspired engineering is that the spicules are a poor model material system for the purposes of enhancing fracture toughness in synthetic composites, and investigation or formulation of mechanisms that connect the spicules' architecture to fracture toughness enhancement mechanisms should be undertaken with caution. We present our argument in the remainder of this section.

There have been studies that took a closer look at whether the spicules' fracture toughness indeed benefits from their architectures. In addition to the similarity between the architectures of prototypically tough SBMs and spicules, studies such as those by Levi et al. (1989) and Sarikaya et al. (2001) are most prominently cited to intimate that the spicules' fracture toughness is enhanced by their internal architectures (Sundar et al., 2003; Aizenberg et al., 2004; Mayer, 2005; Weaver et al., 2007; Walter et al., 2007; Müller et al., 2008). Both studies involve three-point bending tests on spicules—of *Monorhaphis chuni* sponge in the study by Levi et al. and of *Rosella racovitzae* sponge in the study by Sarikaya et al. They observe that in their tests, (o.1) the “fracture energy,” as estimated by the area under the force-displacement/stress-strain curve, is higher in the spicules than in monolithic silica rods of similar diameters, and (o.2) the force-displacement/stress-strain curves display “sawtooth patterns.” The force-displacement curve from the work by Levi et al. and the stress-strain curve from the work by Sarikaya et al. are shown in Fig. 4(A) and (C), respectively.

The area under the force-displacement/stress-strain curve, or to be more precise, the area enclosed by force-displacement/stress-strain curve in a load-unload cycle, in tests such as those conducted by Levi et al. and Sarikaya et al., can only provide upper bounds on fracture toughness. In order to be able to use the area enclosed by the force-displacement/stress-strain curve to construct meaningful measures of fracture toughness, such as the work of fracture (WOF), it is critical that, at the very least, the following two criteria be satisfied in the tests: (c.1) the specimen's failure takes place through the growth of a clearly identifiable dominant crack whose geometry, at least after complete failure, can be clearly ascertained, and (c.2) the dominant crack grows in a stable³ manner. Otherwise, the work done by the loading mechanism, which is what the area enclosed by the force-displacement/stress-strain curve

² Not all spicules have layered architectures, nor do they have a fiber or rod-like appearance. In this paper we only focus on the particular variety of spicules that are both layered and have a fiber or rod-like appearance. For this reason and for the sake of simplicity of exposition, we refer to this special category of spicules as just spicules.

³ By which we mean that the crack's geometry changes slowly, such that the specimen's velocity field is of negligible magnitude, and continuously, such that there are no abrupt or sudden changes in the crack's geometry, with the loading. Sarikaya et al. state that the crack propagation was stable in their study as well. They make this comment in reference to the punctuated manner in which their specimen fails, i.e., to the presence of sawtooth patterns in their force-displacement curves. Thus, their definition of “stable crack growth” is quite different from that of ours.



represents, goes into not only growing the dominant crack but also feeding the specimen's kinetic as well as other forms of energies. These eventually get dissipated by inelastic mechanisms different from those that operate in the dominant crack's fracture process zone. The criteria (c.1)–(c.2) have not been met in the tests by Levi et al. and Sarikaya et al., and the upper bounds of fracture toughness being higher in the spicules compared to homogenous reference structures does not necessarily mean that the true fracture toughness is also higher in the spicules.

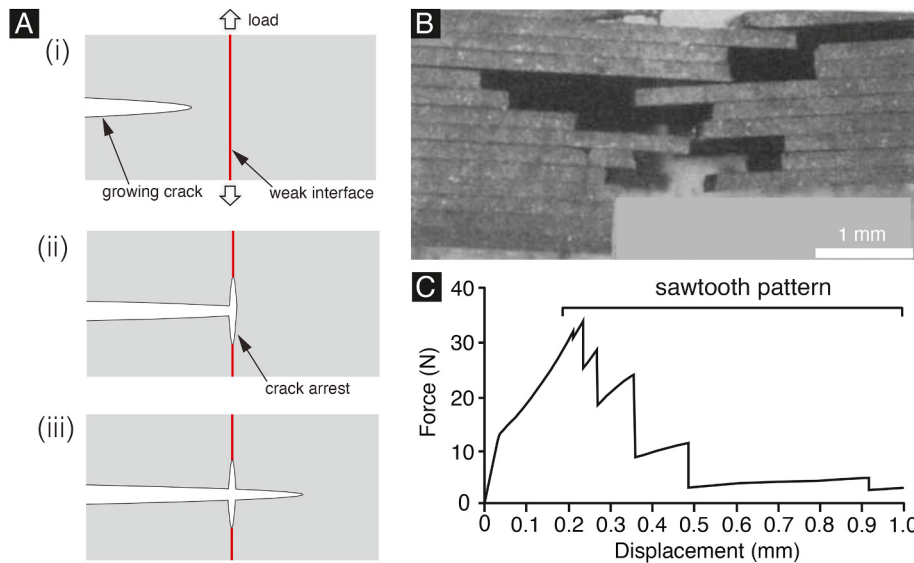
Monn et al. adhered to the criteria (c.1)–(c.2) in their three-point bending tests on *Ea*. spicules. They showed that the spicules' fracture toughness, at least in the case of *Ea*. spicules, is not substantially greater than that of reference homogenous structures. They argue that the reason why the *Ea*. spicules do not display the remarkable toughness enhancement seen in prototypically tough SBMs, despite possessing an architecture that is quite similar to theirs, is because the spicules' architecture differs from those of prototypically tough SBMs in an important aspect: the layers in spicules are curved while those in prototypically tough SBMs are flat. They demonstrated through computational fracture mechanics simulations that the curvature in the spicules' layers essentially shuts down the Cook-Gordon mechanism.

As pointed out above, the increase in areas enclosed by the load-displacement curves does not necessarily mean increased fracture toughness, and the work by Monn et al. shows that the internal

architectures of spicules should not be treated as equivalent in function to those of the prototypically tough SBMs. Nevertheless, the observation of the sawtooth patterns in tests such as those conducted by Levi et al. and Sarikaya et al. can still incline one to expect toughness enhancement in the spicules; that is, if there is no substantial toughness enhancement in the spicules,⁴ then how does one explain the sawtooth patterns in tests such as those conducted by Levi et al. and Sarikaya et al. In order to further support the claim by Monn et al. that there is insignificant toughness enhancement in spicules, we present here experiments that show that there can be other explanations for the spicules' sawtooth pattern, instead of them necessarily having to be the result of the Cook-Gordon mechanism. Specifically, we show that the sawtooth patterns can be due to a sequence of slip events that take place at the supports in the bending tests.

In a standard three-point bending test, a specimen is placed on a mechanical testing stage whose supports consist of either two rollers or "knife edges" that are set a fixed distance apart (see Fig. 5). The standard set-up for the three-point bending test is called the simply-supported

⁴ Some spicules which differ from the rest substantially in terms of size, function, and architectures, such as *M. chuni*, may be an outlier to this claim. We will discuss this point further in the conclusion.



imen was higher than that of a homogenous silicon carbide specimen. It was observed that the graphite-coated interfaces of the Cook-Gordon mechanism, in that they repeatedly deflected/trapped the growing crack; this can be gleaned from the image. (C) shows a representative force-displacement curve from the work by Clegg et al. (modified with permission from Clegg et al., 1990; copyright 1990 Springer Nature).

(SS) set-up, in which the specimen is not affixed to the mechanical testing stage and is therefore free to slip at the supports (cf. Fig. 6). Typically, the deflection of engineering materials that get tested this way is small enough such that the slip at the supports is minimal. However, for slender samples with large spans—often the case with tests on very small specimens like the spicules—the deflections and consequently the slip can be much larger.

We performed three-point bending tests on *Ea* spicules, which closely resemble the spicules from *M. chuni* and *R. racovitzae* studied in the works by Levi et al. and Sarikaya et al., respectively. The details of how we prepared the *Ea* spicules for testing are given in § 2.2 and the methodology of our experiments is discussed further in § 2.3. As Levi et al. and Sarikaya et al. did in their respective experiments, we also observed sawtooth patterns in the force-displacement ($F-w_0$) curves of our experiments. These results are presented in § 3.1.1, and, e.g., in Fig. 7(A). However, in addition to what is usually done in three-point bending tests on spicules, we also measured the arc length, which is the length of the section of the spicule specimen lying between the supports during the test (see Fig. 8(A)). We found that at the very instance when there is a sudden drop in force, there is also a sudden increase in the arc length. This observation implies that during each force-drop event, there also occurs a slip event at the supports in the experiment.

We try to interpret our observation of a slip event co-occurring with each force-drop event by considering the following hypotheses: (h.1) each force drop is entirely due to a layer-fracture event, i.e., while slip events correlate with the force-drop events they do not cause them, (h.2) the force drops are due to a combination of layer-fracture and slip events, or (h.3) a force drop is entirely due to its co-slip event.

In order to investigate the above hypotheses, we repeated the *Ea* bending tests but this time keeping the spicule ends fixed by gluing them to the mechanical testing stage (see Fig. 6). This new set-up, which we refer to as the fixed-fixed (FF) set-up, prevents any potential slip events during the bending test but is not expected to affect the Cook-Gordon mechanism. Thus, if (h.1) is true then the sawtooth patterns should appear in these FF experiments as well. Alternatively, if (h.2) is true then the force drops in the sawtooth patterns should decrease in magnitude, and finally, if (h.3) is true then the sawtooth patterns should completely

Fig. 2. Cook-Gordon mechanism. (A) In the Cook-Gordon mechanism, a growing crack (see (i)) is repeatedly arrested. This arrest takes place via the crack getting deflected towards or trapped in directions that quickly reduce the crack driving force, as illustrated in (ii). The deflection or trapping is caused by the crack encountering weak interfaces whose strengths and orientations lie within certain ranges (Ming-Yuan and Hutchinson, 1989). As the loading is continued, the crack re-initiates, sometimes by sprouting a new growing tip from its fracture surfaces (see (iii)). The above process repeats itself each time the crack encounters the right type of weak interface. The repeated arrest and re-initiation causes the crack to consume more energy than what it would have consumed if it were to traverse the same nominal path without any interruptions. (B) shows a fractured specimen from the work by Clegg et al. (modified with permission from Clegg et al., 1990; copyright 1990 Springer Nature). Taking inspiration from the prototypically tough SBM, nacre, the specimen was designed to have layered architecture that consisted of a stack of silicon carbide layers coated with graphite. This nacre-mimic specimen displayed fracture toughness enhancement—i.e., in three-point bending tests, the fracture toughness of the spec-

imen was higher than that of a homogenous silicon carbide specimen. It was observed that the graphite-coated interfaces of the Cook-Gordon mechanism, in that they repeatedly deflected/trapped the growing crack; this can be gleaned from the image. (C) shows a representative force-displacement curve from the work by Clegg et al. (modified with permission from Clegg et al., 1990; copyright 1990 Springer Nature).

vanish. The $F-w_0$ curves from the FF set-up tests are shown in Figs. 7(B) and 9 and discussed in § 3.1.2. As can be seen from the figure, the sawtooth patterns completely vanish, implying that (h.3) is true, i.e., that the sawtooth patterns in our SS set-up experiments are not due to the Cook-Gordon mechanism but due to slip events.

One way in which our above reasoning could be flawed is if our assumption that the FF set-up does not affect the operation of the Cook-Gordon mechanism is false. In such case, our FF set-up experiments do not irrefutably support the interpretation that the sawtooth patterns in our SS set-up experiments are solely due to slip events. Therefore, we investigated the hypotheses (h.1)–(h.3) through a different means as well.

We repeated the bending tests for a second time. We carried out these tests in the SS set-up as we did with the first bending tests, but this time we loaded, unloaded, and then re-loaded the same specimen. Specifically, we loaded the specimen and stopped the loading before the specimen failed. We then completely unloaded the specimen until the force became close to zero and the specimen almost regained its straight shape. The $F-w_0$ curves from these tests consisting of such load-unload cycles, which we refer to as the load-unload tests, are presented in § 3.2 and shown in Fig. 10. If layer-fracture events had any role in the sawtooth pattern observed during the loading phase of the first cycle, then the slope of the linear portion of the $F-w_0$ curve in the first cycle's unloading phase, as well as in the loading or unloading phases of any of the subsequent cycles, would be smaller than the slope in the loading phase of the first cycle. This is because crack growth invariably decreases a structure's elastic stiffness. In Fig. 10(B) we see that the slopes in the first unloading phase and the second loading phase are quite similar to the slope in the first loading phase. Thus, the load-unload tests also imply that the sawtooth patterns in our SS set-up experiments are due to slip events, i.e., that (h.3) is true.

As we did in the case of our argument based on the FF set-up experiments, we can think of ways in which our argument based on the load-unload tests is also flawed. However, our arguments based on the FF set-up experiments and the load-unload tests when taken in conjunction make it quite unlikely that (h.3) is untrue.

The hypothesis (h.3) likely being true means that sawtooth patterns from flexural tests should not implicitly be taken to be evidence for the

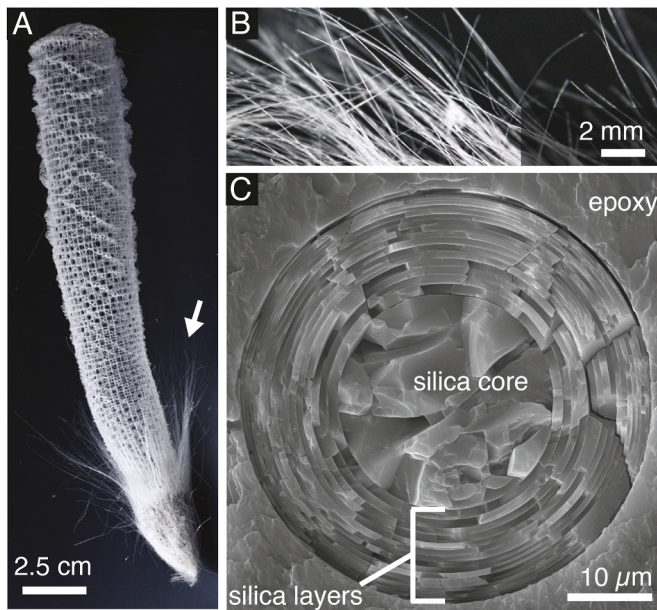


Fig. 3. Structure of *Euplectella aspergillum* (*Ea.*) sponge and its basalia spicules. (A) The entire skeletal structure of a *Ea.* sponge is shown (modified from (Monn et al., 2015); copyright 2015 National Academy of Sciences). The basalia spicules, which are identified with a white arrow, are around $50 \mu\text{m}$ in diameter and can be several centimeters long. (B) A magnified view of the basalia spicules (modified from (Monn et al., 2015); copyright 2015 National Academy of Sciences). (C) An SEM image showing the cross section of a *Ea.* basalia spicule reveals its cylindrically layered internal architecture (modified from (Monn et al., 2015); copyright 2015 National Academy of Sciences). The internal architecture is relatively consistent between different spicules, as have been found through investigation of a large number of *Ea.* spicules in a previous study (Monn et al., 2015). In general, a *Ea.* spicule's internal architecture consists of a cylindrical silica core of about $10 \mu\text{m}$ radius surrounded by approximately 25 concentric, cylindrical silica layers. The thicknesses of the cylindrical silica layers decrease from $\approx 1.2 \mu\text{m}$ to $\approx 0.3 \mu\text{m}$ as one moves away from the core. This decrement pattern has previously been measured and investigated for its functional significance in (Monn et al., 2015). Between the silica core and the innermost cylindrical silica layer, as well as between adjacent cylindrical silica layers, there are compliant organic layers whose thickness are, roughly, in the 5–10 nm range (Weaver et al., 2007).

operation of the Cook-Gordon or other material toughening mechanisms. Our work underscores the point that it is better to ascertain the fracture toughness enhancement by measuring the material's fracture toughness directly by carrying out tests that adhere to criteria such as (c.1)–(c.2), rather than relying on visual similarities between the material's and the prototypically tough SBMs' architectures, or on sawtooth type features in the force-displacement curves. We make further remarks on the implications of our work in § 4.

2. Materials and methods

2.1. Mathematical and theoretical mechanics preliminaries

In this subsection we briefly recap a few important mathematical and theoretical-mechanics-related notions that are necessary for a clear description of our experiments, and their interpretation and discussion.

We assume that our experiment takes place in \mathcal{E} , a three dimensional physical point space. Let \mathbb{E} be a three dimensional, oriented, Hilbert space such that \mathcal{E} is \mathbb{E} 's principle homogenous space. We take the vectors $\hat{\mathbf{l}}_1$, $\hat{\mathbf{l}}_2$, and $\hat{\mathbf{l}}_3$, which are shown marked in Fig. 5(A), to form a basis for \mathbb{E} . We denote the dot product between any two vectors \mathbf{u} and \mathbf{v} as $\mathbf{u} \cdot \mathbf{v}$. It follows from the definition of the inner-product that $\mathbf{u} \cdot \mathbf{v} \in \mathbb{R}$, where \mathbb{R} is the set of all real numbers. The vectors $\hat{\mathbf{l}}_1$, $\hat{\mathbf{l}}_2$, and $\hat{\mathbf{l}}_3$ are orthonormal,

which is to say that $\hat{\mathbf{l}}_i \cdot \hat{\mathbf{l}}_j = \delta_{ij}$, where $i, j \in (1, 2, 3)$ and δ_{ij} is the Kronecker delta symbol. The Kronecker delta symbol, δ_{ij} , is defined such that δ_{ij} equals unity if $i = j$ and naught otherwise.

Following (Rahaman et al., 2020), we take that vectors that belong to a physical vector space carry units with them. For instance, we take that $\hat{\mathbf{l}}_i$, $i \in (1, 2, 3)$, carry the units of μm (micrometers) with them. We denote the magnitude of the vector \mathbf{u} as $\|\mathbf{u}\|$. We only deal with Hilbert spaces in this paper and take $\|\mathbf{u}\|$ to be equal to $(\mathbf{u} \cdot \mathbf{u})^{1/2}$. Consequently $\|\mathbf{u}\|$ is non-dimensional, or to be more precise $\|\mathbf{u}\| \in \mathbb{R}_{\geq 0}$, where $\mathbb{R}_{\geq 0}$ is the set of non-negative real numbers.

Following (Rahaman et al., 2020) and (Deng and Kesari, 2004), we model force as a linear map from \mathbb{E} into a one dimensional vector space whose elements have units of energy. The set of all forces that act on the matter contained in \mathcal{E} can be made into a Hilbert space. We denote that vector space as \mathbb{F} . We use the orthonormal set $(\hat{\mathbf{f}}_i)_{i \in (1, 2, 3)}$ as a basis for \mathbb{F} .

The vectors $\hat{\mathbf{f}}_i$, $i \in (1, 2, 3)$, are defined such that they carry the units of mN (millinewtons) and $\hat{\mathbf{f}}_i(\hat{\mathbf{l}}_j) = \delta_{ij} \text{ nJ } (10^{-9} \text{ Joules})$.

From here on we will be denoting lists such as $\hat{\mathbf{l}}_1$, $\hat{\mathbf{l}}_2$, and $\hat{\mathbf{l}}_3$ and $\hat{\mathbf{f}}_j$, $j \in (1, 2, 3)$, simply as $\hat{\mathbf{l}}_i$ and $\hat{\mathbf{f}}_j$, respectively, and ordered sets such as $(\hat{\mathbf{l}}_i)_{i \in (1, 2, 3)}$ simply as $(\hat{\mathbf{l}}_i)$.

2.2. Materials

Euplectella aspergillum skeletons were purchased from a commercial supplier in a dried state with the organic tissue already removed (see Fig. 3(A)) and were stored in dry conditions at room temperature. We carefully removed *Ea.* spicules from the skeletons using a pair of tweezers and inspected them under a polarized light microscope. Sections of the spicules containing barbs and any other sections that were visibly damaged or had rough, cracked surfaces were discarded. Immediately before performing experiments, we cut the spicules into $\approx 5 \text{ mm}$ long sections using a razor blade in order to mount them onto a mechanical testing stage. The mounted $\approx 5 \text{ mm}$ long spicule sections can be seen in Figs. 5(C) and 6(C). In some experiments the spicules were fixed to the testing device using a solvent-based, drying adhesive (TED PELLA, INC., California, U.S.A., PELCO® Conductive Carbon Glue). In Fig. 6(A) and (B), we mark the regions where the adhesive was applied using transparent green rectangles. The schematic shown in Fig. 6(B) corresponds to the optical micrograph shown in Fig. 6(C). Unfortunately, the adhesive is not clearly visible in Fig. 6(C).

2.3. Experimental procedure and measurements

2.3.1. Measurement of force-displacement, $F-w_0$, curves

We performed force-displacement measurement experiments on a number of spicule specimens using a custom-built mechanical testing system. The construction and operation of the mechanical testing system is described in detail in (Monn and Kesari, 2017) and (Monn et al., 2017). A force-displacement experiment consisted of loading phases and unloading phases. We will explain the physical quantities force and displacement that we used while referring to our experiments shortly in the following paragraphs. We will also explain what we mean by loading and unloading phases later in this sub-section.

In a force-displacement experiment a spicule specimen was initially placed across a trench that was cut into a steel plate. The trench's geometry and the spicule specimen's initial orientation and position with respect to the trench are sketched in Fig. 5(A). The trench was straight and ran along the $\hat{\mathbf{l}}_3$ direction. It had a rectangular profile (see Fig. 5(A)). The spicule specimen was placed across the trench such that initially it lay along the $\hat{\mathbf{l}}_1$ direction. We performed the experiments in

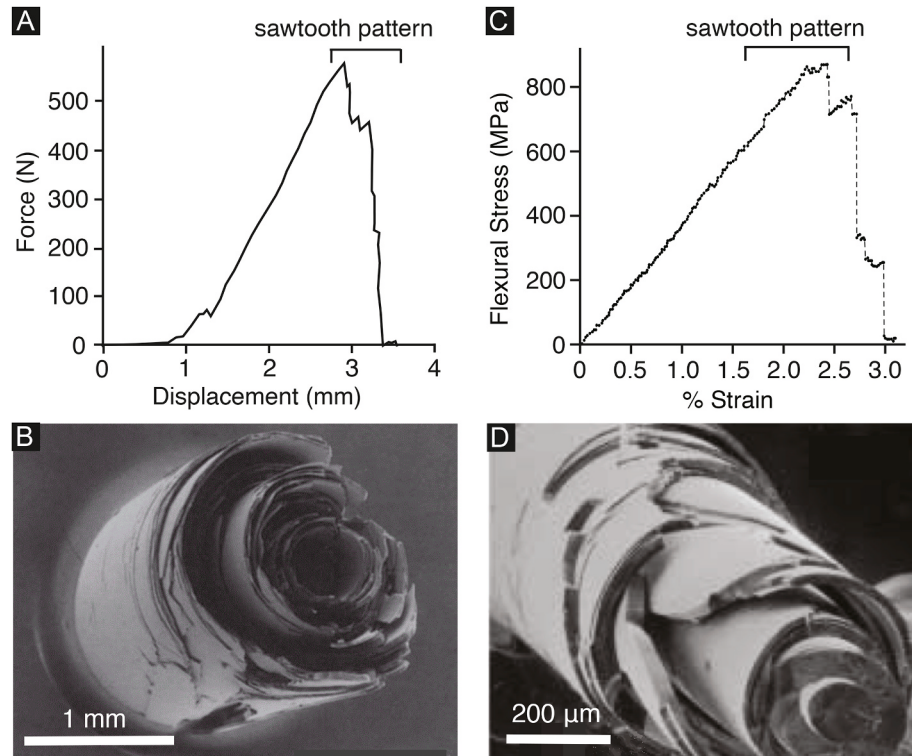


Fig. 4. (A) A force-displacement curve from a three-point bending test performed on a *Monorhaphis chuni* anchor spicule (modified with permission from (Levi et al., 1989); copyright 1989 Springer Nature). (B) An image of a fractured *M. chuni* anchor spicule (modified with permission from (Levi et al., 1989); copyright 1989 Springer Nature). (C) A stress-strain curve from a three-point bending test performed on a *Rosella racovitzae* spicule (modified with permission from (Sarikaya et al., 2001); copyright 2001 Springer Nature). (D) An image of a fractured *R. racovitzae* spicule tested in three-point bending (modified with permission from (Tamerler and Sarikaya, 2009); copyright 2009 The Royal Society (U.K.)).

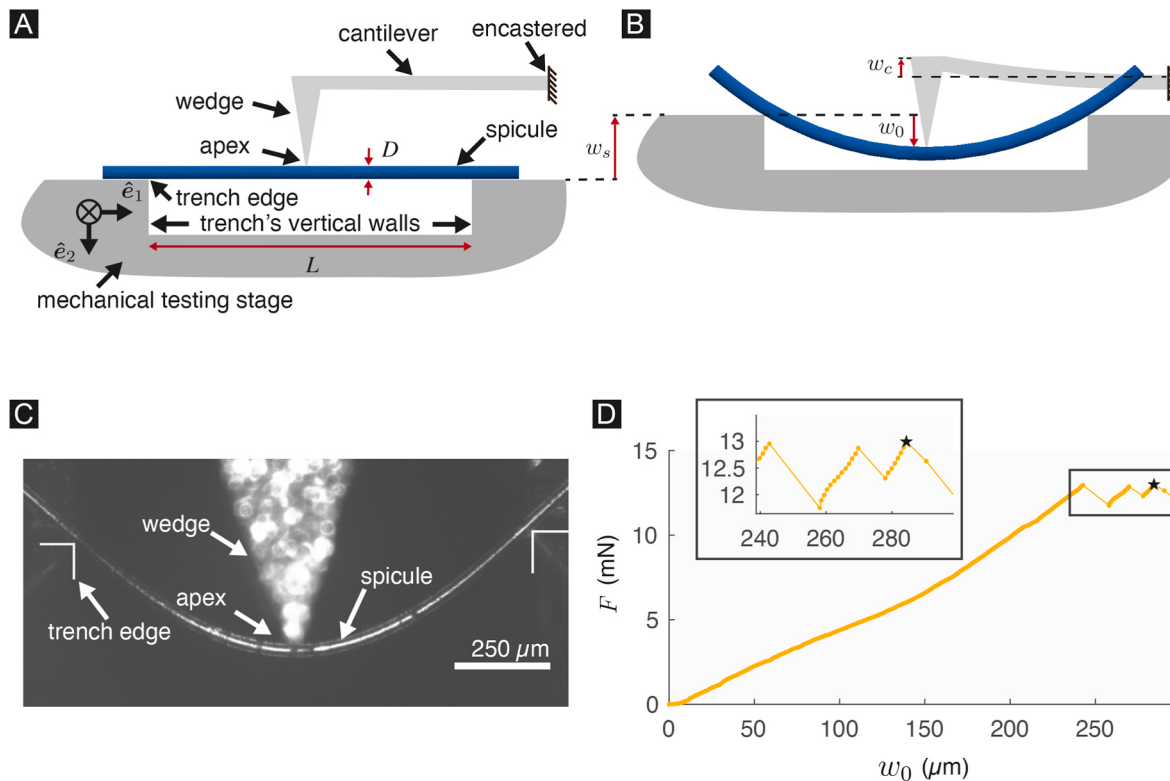


Fig. 5. Description of three-point bending test set-ups and data obtained from the tests. (A) and (B) are schematics of the simply-supported (SS) set-up of the experiments. The spicule is suspended over a trench, loaded at its mid-span by a wedge attached to a cantilever. Schematic (A) shows the reference configuration, while schematic (B) shows the deformed configuration. The mid-span specimen deflection, w_0 , cantilever displacement, w_c , and stage displacement, w_s , are marked in (A) and (B). Basis vectors \hat{e}_1 and \hat{e}_2 are shown in (A). Basis vector \hat{e}_3 points into the plane of the schematic. (C) A micrograph of the spicule's deformed configuration in the SS set-up. (D) The force-displacement ($F-w_0$) curve for a representative spicule tested in the SS set-up. The inset shows a zoomed-in view of the boxed region. The star marks the point after which the force between the spicule and the cantilever vanishes.

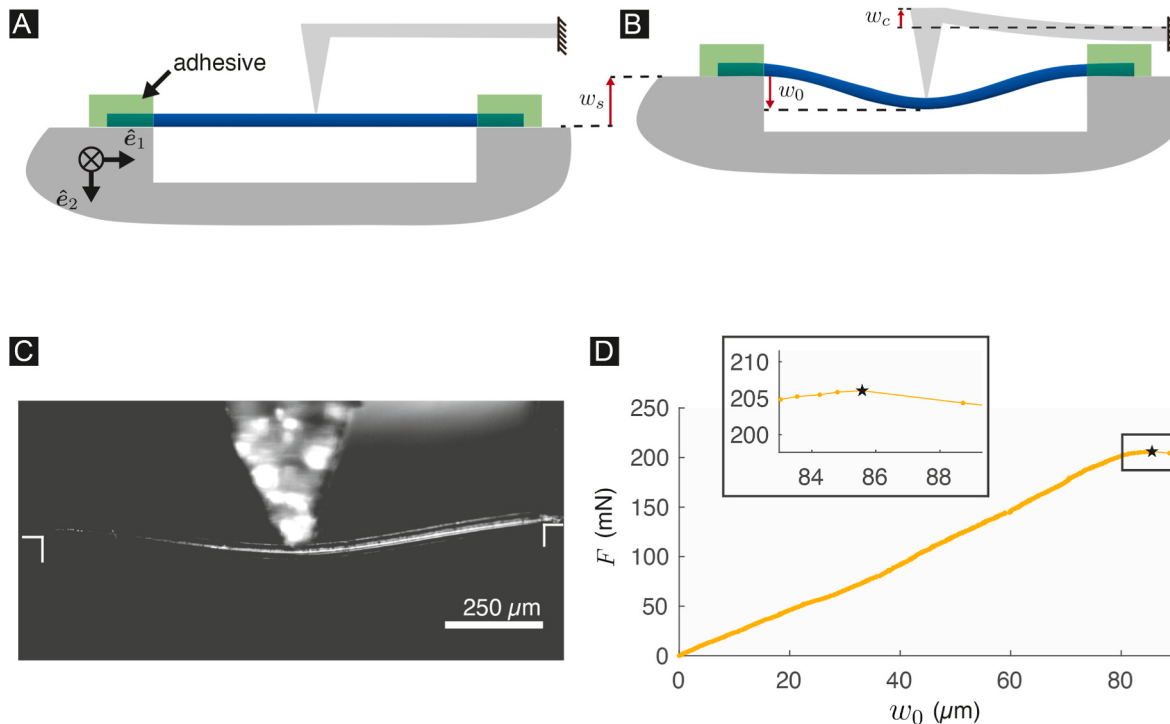


Fig. 6. Description of three-point bending test set-ups and data obtained from the tests. (A) and (B) are schematics of the fixed-fixed (FF) set-up of the experiments. In contrast with the simply-supported test set-up, an adhesive is applied over the spicule's ends to prevent it from sliding or rotating during the test. Schematic (A) shows the reference configuration, while schematic (B) shows a deformed configuration. The mid-span specimen deflection, w_0 , cantilever displacement, w_c , and stage displacement, w_s are marked in (A) and (B). Basis vectors \hat{e}_1 and \hat{e}_2 are shown in (A). Basis vector \hat{e}_3 points into the schematic. (C) A micrograph of a spicule's deformed configuration in the FF set-up. (D) The force-displacement (F - w_0) curve for a representative spicule tested in the FF set-up. The inset shows a zoomed-in view of the boxed region. The star on the F - w_0 curve marks the point after which the force between the spicule and the cantilever vanishes.

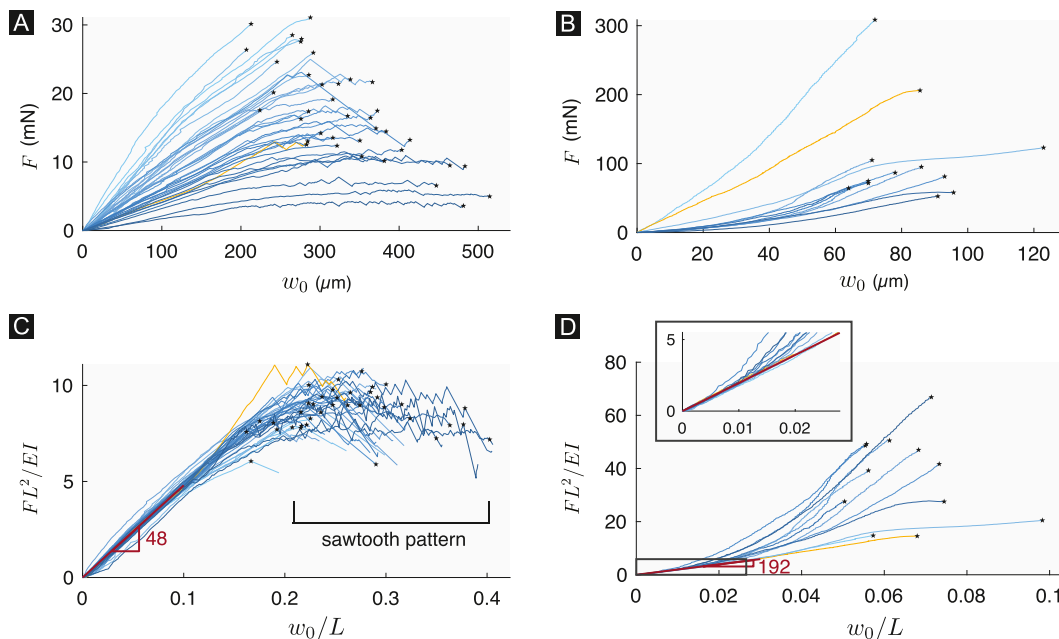


Fig. 7. (A) Force-displacement curves for 38 *Ea.* spicules tested in the simply-supported set-up. This data includes the 33 *Ea.* spicules previously tested in (Monn and Kesari, 2017). (B) Force-displacement curves for 12 *Ea.* spicules tested in the fixed-fixed set-up. (C) and (D) show scaled versions of the force-displacement curves shown in (A) and (B), respectively. The scaled force-displacement curves are defined in § 2.3.2. The force-displacement curves shown in Figs. 5(D) and 6(D) are shown in orange in (A) and (B), respectively, and their scaled versions are shown in orange in (C) and (D), respectively. In (C) and (D) the initial portions of the scaled curves match well with the predictions of the Euler-Bernoulli beam theory, which are shown in dark-red (see the paragraphs around (8) and (10) for details). The black stars in (A)–(D) indicate the force and displacement just before the specimen fails, i.e., just before the force vanishes.

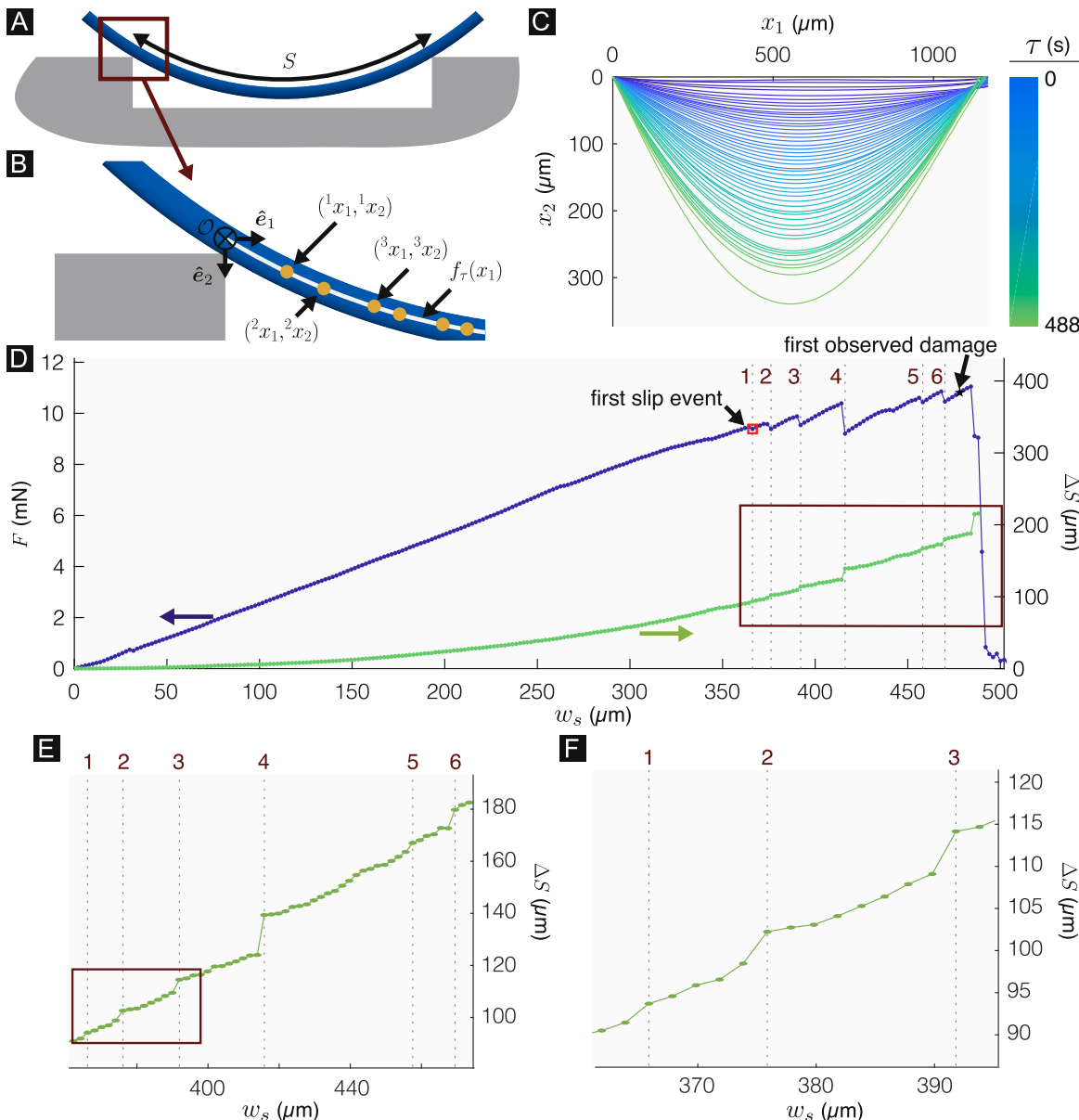


Fig. 8. Correlation between the sawtooth pattern in the force-displacement response and discontinuous jumps in arc length. (A) A schematic of a spicule's deformed configuration in the simply-supported set-up showing the arc length S . (B) Magnified view of the boxed region in (A) showing the points $(^i x_1, ^i x_2)_{i=1\dots n}$ identified along the spicule's longitudinal axis and the graph of $f_r : [0, L] \rightarrow \mathbb{R}$, which is our analytical representation of the longitudinal axis. (C) The graph of the function f_r for a representative spicule computed after every fifth stage displacement increment. (D) The force, F , (left axis) as a function of stage displacement, w_s , for a representative spicule compared to the total change in arc length ΔS (right axis). The vertical, dashed lines indicate the w_s values at which we identified discontinuities (numbered 1–6) in the $F-w_s$ curve. (E) A zoomed-in view of the plot region within the red rectangle in (D). (F) A zoomed-in view of the plot region within the red rectangle in (E) highlighting the discontinuous changes in ΔS at locations 1–3.

one of the following two set-ups: (i) Simply-supported (SS, see Fig. 5(A), (B)), and (ii) Fixed-Fixed (FF, see Fig. 6(A), (B)). In the simply-supported set-up the spicule specimen was placed across the trench without any efforts on our part to affix it to the steel plate. Therefore, in this set-up, the specimen was able to slide-across as well as rotate-about the trench edges (see Fig. 5(A), (B)). The SS (simply-supported) set-up has been used in previous experiments performed on the *Ea* spicules by the current authors (Monn and Kesari, 2017) as well as by other researchers (Walter et al., 2007). In the FF (fixed-fixed) set-up, after the spicule specimen was placed across the trench, its ends were fixed to the steel plate using an adhesive (see § 2.2 for details) so that they could not slip-across or rotate-about the trench edges (see Fig. 6(A), (B)). Specimens loaded onto the steel plate in the FF set-up were inspected again after the application of the glue to ensure that the glue covered the ends

of the spicule only up to the trench edges, and did not cover any portions of the specimen that remained suspended over the trench.

The steel plate with trenches cut on it, which we will henceforth refer to as the mechanical testing stage (MTS), was controlled using a three-axis actuator. Before beginning each experiment, the MTS was positioned so that the spicule was beneath an aluminum wedge and the wedge's apex was located mid-way across the trench (e.g., see Fig. 5(A)). The wedge was part of a larger, passive, mechanical structure that we call the cantilever (Fig. 5(A)). The wedge composed the cantilever's left free end. That is, in the parlance of Atomic Force Microscopy (AFM) experiments (Kesari et al., 2010), the wedge was the cantilever's tip. The cantilever's right end was encastered into a rigid aluminum frame, which was bolted on to an optical table. The cantilever's material and dimensions varied between the experiments. In some experiments, we

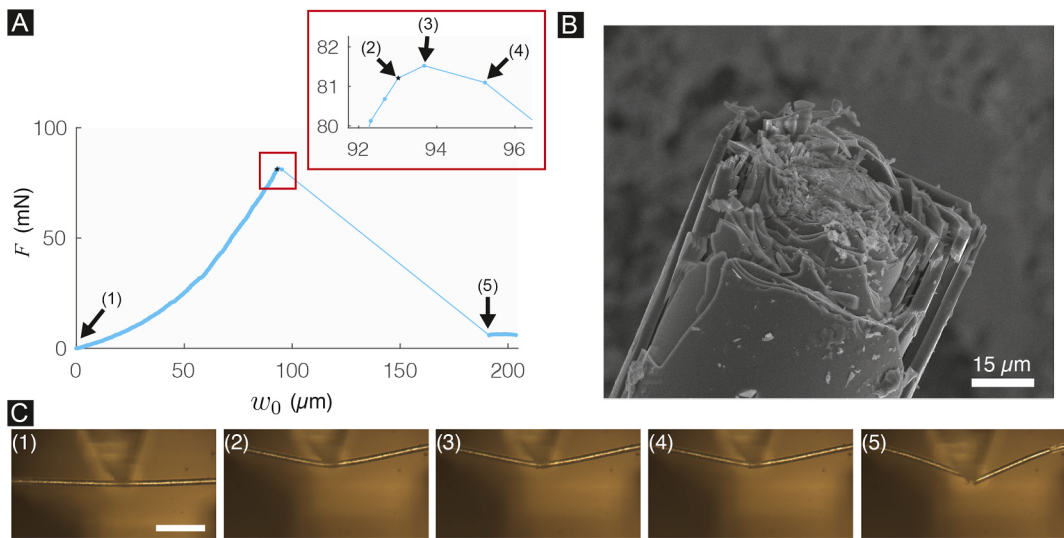


Fig. 9. Specimen failure in a representative fixed-fixed set-up failure test. (A) The force F as a function of mid-span specimen displacement w_0 for a representative spicule tested in the fixed-fixed set-up. The inset shows a zoomed view of the plot region within the red square. (B) A micrograph of the broken end of the spicule whose F - w_0 curve is shown in (A). (C) Optical micrographs taken during different stages of the failure test. The micrograph numbers (1)–(5) correspond to the similarly numbered (w_0 , F) points shown in (A). The scale bar in (1) measures 250 μm and micrographs (2)–(5) have the same scale as (1). In (1), the spicule is in the reference configuration. Images (2)–(4) show the spicule while it is in the process of failing; image (5) shows the spicule after it has failed completely. The failure process ((2)–(4)) occurs over only two stage displacement increments and does not display the sawtooth pattern observed in the tests performed in the simply-supported set-up (see Figs. 5(D), 7(A), (C) and 8(D)).

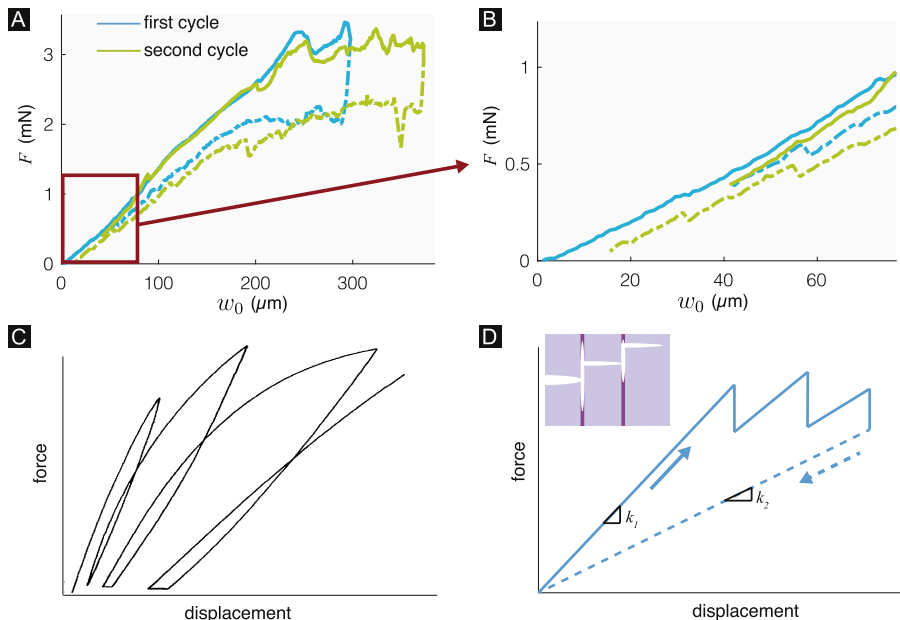


Fig. 10. Force-displacement curves from simply-supported load-unload tests. (A) The force-displacement curve from the first two cycles of a representative load-unload test carried on a *Ea*. spicule in the simply-supported set-up (see § 3.2 for details). The blue and green parts of the curve correspond to the first and second load-unload cycles, respectively. The loading and unloading portions of the curves are shown using solid and dashed lines, respectively. (B) shows a zoomed-in view of the region in (A) that is marked using a dark-red rectangle. (C) Force-displacement curves from the first three load-unload cycles and the loading portion of the fourth cycle of a three-point bending load-unload test, of the type that we discuss in § 3.2, carried out on a nacre specimen from *Pinctada margaritifera* (modified with permission from (Currey, 1977); copyright 1977 The Royal Society (U.K.)). (D) A schematic representation of the F - w_0 curve of a material that experiences a sequence of crack arrest and re-initiation. The inset schematically depicts the crack path that results from repeated crack arrest and growth in a material (lavender) that contains thin interlayers (purple). The vertical segments in the loading branch are force drops that begin and end with the sudden growth and arrest of the crack, respectively. The schematic also illustrates that upon unloading, the stiffness k_2 of the damaged specimen is smaller than the stiffness k_1 of the undamaged specimen (Ouchterlony, 1981; Bush,

1976).

used an aluminum cantilever, while in others, we used a stainless steel cantilever. However, in the context of our experiments, only the cantilever's stiffness κ_c —which we will define shortly, later in this subsection—is relevant. We report the stiffness of the cantilever in each of our experiments in Tables S1–S4 in the Supplementary Information. As can be noted from these tables, the cantilever stiffnesses in our experiments varied between 86.4 N/m and 1800.2 N/m. The methodology of how we measured those stiffnesses is described in (Monn et al., 2017).

As we mentioned previously, each of our force-displacement mea-

surement experiments consisted of loading and unloading phases. The experiments were carried out by moving the MTS, which carried the spicule specimens, in increments of 1 μm at a rate of 1 $\mu\text{m/sec}$. In a loading phase, the MTS was moved towards the cantilever, i.e., in the $-\hat{\tau}_2$ direction. In an unloading phase, the MTS was moved away from the cantilever, i.e., in the $\hat{\tau}_2$ direction. During the loading phase, assuming the spicule remains unbroken, the spicule comes into contact with the cantilever's tip and then gets deformed as the tip presses into it; the

cantilever gets deformed during this process as well (cf. subfigures (A) and (B) in either Fig. 5 or 6). The reference configurations we choose for the spicule specimen and the cantilever, in which they are undeformed, are shown in Fig. 5(A) and 6(A) for the SS and FF set-ups, respectively. Representative deformed configurations of the spicule specimen and the cantilever in the SS and FF set-ups are shown in Fig. 5(B) and 6(B), respectively.

The MTS's displacement at the (non-dimensional) time instance $\tau \in \mathbb{R}_{\geq 0}$ corresponding to the just described motion and the reference and deformed configuration can be denoted as $-w_s(\tau)\hat{\gamma}_2$, where $w_s(\tau) \in \mathbb{R}$. We take that $\tau = 0$ at the instance when the tip first makes contact with the spicule. When there is no risk of confusion we refer to the non-dimensional quantity $w_s(\tau)$ itself as the MTS's displacement. Since the MTS's motion is our input to the experiment we know the function $\mathbb{R}_{\geq 0} \ni \tau \mapsto w_s(\tau) \in \mathbb{R}$ in each experiment.

We call the dot product between the displacement vector of the apex of the cantilever's tip at the time instance τ and $-\hat{\gamma}_2$ the (non-dimensional) cantilever displacement at time τ and denote it as $w_c(\tau) \in \mathbb{R}$. We assume that the force applied on the spicule specimen by the cantilever's tip acts in the $\pm\hat{\gamma}_2$ directions. That is, to be mathematically precise, we assume that the force at the time instance τ has the form $F(\tau)\hat{f}_2$, where $F(\tau) \in \mathbb{R}$. We call the quantity $F(\tau)/w_c(\tau)$ in the limit of $\tau \rightarrow 0$ the non-dimensional cantilever stiffness or, when there is no risk of confusion, simply the cantilever stiffness and denote it as $k_c \in \mathbb{R}$. The (dimensional, or physical) cantilever stiffness κ_c is defined in terms of the non-dimensional cantilever stiffness k_c by the equation $\kappa_c = k_c \text{ mN}/\mu\text{m}$.

In each experiment we measured the function $\mathbb{R}_{\geq 0} \ni \tau \mapsto k_c w_c(\tau) \in \mathbb{R}$. We call the dot product between the displacement vector of the centroid of the spicule's cross-section that is directly underneath the apex of the cantilever's tip and $\hat{\gamma}_2$ the mid-span spicule deflection, or simply displacement, and denote it as $w_0(\tau) \in \mathbb{R}$. It can be shown that the quantities $w_s(\tau)$, $w_c(\tau)$, and $w_0(\tau)$ are related as

$$w_s(\tau) = w_c(\tau) + w_0(\tau). \quad (1)$$

We call the map

$$\mathbb{R}_{\geq 0} \ni \tau \mapsto (F(\tau), w_0(\tau)) \in \mathbb{R}^2 \quad (2)$$

the F - w_0 curve. Initial portions of the F - w_0 curves from representative SS and FF experiments are shown in Fig. 5(D) and 6(D), respectively. These initial portions were taken from the loading phase of the experiments. We will present and discuss other portions of the F - w_0 curves in later sections.

2.3.2. Scaled force-displacement curves

The question of how well the measured F - w_0 curves conform with the predictions of the Euler-Bernoulli beam theory can be answered by preparing scaled versions of the F - w_0 curves. By the scaled version of an F - w_0 curve, we mean the curve

$$\mathbb{R}_{\geq 0} \ni \tau \mapsto \left(\frac{F(\tau)L^2}{EI}, \frac{w_0(\tau)}{L} \right) \in \mathbb{R}^2, \quad (3)$$

where $I \mu\text{m}^4$ is the spicule specimen's bending moment of inertia, $L \mu\text{m}$ is the trench width, and $E \text{ mN}/\mu\text{m}^2$ is the spicule specimen's effective Young's modulus. Thus, creating a scaled F - w_0 curve for an experiment from the experiment's raw F - w_0 curve requires knowledge of E , I , and L in that experiment. We describe how we measured each of these quantities in the next paragraph.

Let the spicule specimen's diameter be $D \mu\text{m}$, where $D \in \mathbb{R}_{\geq 0}$. We measured D in each of our experiments using the scanning electron microscope (SEM) images that were taken following the experiments. Using those measurements we calculated the (non-dimensional) bending moment of inertia I in each of our experiments as $I = \pi D^4/64$. The trench width ($L \mu\text{m}$) is the distance between the trench's vertical walls.

The (non-dimensional) trench width L is shown marked in Fig. 5(A). In our MTS's design L was set to be 1250. However, due to manufacturing variability, L in the actual experiments deviated from this designed value. Therefore, we also measured L in each of our experiments using SEM. The measured D and L values in our experiments are given in Tables S1–S4 in the Supplementary Information. Also given in those tables are the values of the spicule specimen's stiffness in our experiments. A spicule specimen's stiffness k_s is defined as

$$k_s = \lim_{\tau \rightarrow 0} \frac{F(\tau)}{w_0(\tau)}. \quad (4)$$

We measured an experiment's k_s by using that experiment's F - w_0 curve and applying the definition (4). Using the measured I , L , and k_s values we estimated the spicule specimen's (non-dimensional) Young's modulus E in our experiments that were carried out in the SS set-up as

$$E = \frac{k_s L^3}{48I}, \quad (5)$$

and in those that were carried out in the FF set-up as

$$E = \frac{k_s L^3}{192I}. \quad (6)$$

Equations (5) and (6) follow from application of the Euler-Bernoulli beam theory to the SS and FF set-ups of our experiments, respectively [see, e.g., (Gere, 2004), pp. 610 and 717].

2.3.3. Measurement of the length of the spicule section lying between the trench edges: spicule arc length

After each stage displacement increment we imaged the spicule using a reflected light microscope (see e.g. Fig. 5(C) or 6(C)). Using those images, for each spicule specimen we computed the spicule's arc length, which is the length of its segment lying between the trench edges (see Fig. 8(A)) as a function of time.

Specifically, we computed the arc length $S(\tau)$ as

$$S(\tau) = \int_0^L \sqrt{1 + f'_\tau(x_1)^2} dx_1, \quad (7)$$

where $f'_\tau(x_1) = \frac{d}{dx_1} f_\tau(x_1)$ and the function $f_\tau : [0, L] \rightarrow \mathbb{R}$ is defined such that $f_\tau(i x_1(\tau)) = i x_2(\tau)$, where $x_{1i}(\tau)\hat{\gamma}_1 + x_{2i}(\tau)\hat{\gamma}_2$ is the position vector at the time instance τ of a spicule material particle $i\mathcal{X}$ that belongs to the spicule's neutral plane.⁵ In a deformed configuration, the material particle $i\mathcal{X}$ occupies a spatial point in the Euclidean point space \mathcal{E} , which we have defined in § 2.1. The origin of \mathcal{E} is shown marked as \mathcal{O} in Fig. 8(B). We approximated f_τ by fitting a fourth order polynomial to a set of points that lay on the spicule's neutral plane in the spicule's deformed configuration at the time instance τ (see Fig. 8(B)). The graph of f_τ from a representative test is shown after every fifth stage displacement increment in Fig. 8(C).

3. Results

3.1. Failure tests

The failure tests involved a single pair of loading and unloading phases, in which the loading phase was carried out until specimen failure.

⁵ The concept of a neutral plane comes from the engineering theory of beams. In the context of our experiments, roughly speaking, the neutral plane is the set of all spicule material particles that in the spicule's reference configuration belong to the spicule's longitudinal cross-section that contains the spicule's central axis and is normal to the $\hat{\gamma}_2$ direction.

3.1.1. Simply supported set-up

We carried out failure tests in the SS set-up on 5 *Ea.* spicule specimens. Raw $F-w_0$ curves and scaled $F-w_0$ curves from these experiments are shown in Fig. 7(A) and (C), respectively. We show the curves only up to the point of failure, since we deemed the remainder of the curves, i.e., the curves measured post-failure, to be insufficiently interesting and their inclusion to be a distraction from the more important pre-failure portion of the curves. We had previously carried out failure tests in the SS set-up on 33 *Ea.* spicules using the same methodology that we described in § 2.2 and § 2.3 (Monn and Kesari, 2017). We also show the curves from those experiments in Fig. 7(A) and (C).

3.1.1.1. Force-displacement curves and observation of sawtooth patterns.

As can be seen from the figures, initially, the force F increases linearly with the displacement w_0 . For the SS set-up the Euler-Bernoulli theory predicts that the force increases linearly with the displacement as

$$\frac{F(\tau)L^2}{EI} = 48 \frac{w_0(\tau)}{L}. \quad (8)$$

As can be seen from Fig. 7(C) and (8), when w_0/L is smaller than ≈ 0.1 , the measured $F-w_0$ curves match the one predicted by the Euler-Bernoulli beam theory quite well. When w_0/L continues to increase beyond ≈ 0.1 , some of the force-displacement responses start exhibiting nonlinear behavior, and at around $w_0/L \approx 0.18$ ($w_0 \approx 230 \mu\text{m}$) we start to observe sawtooth patterns in several of the $F-w_0$ curves. Specifically, we observed the sawtooth pattern in 22 of the 38 $F-w_0$ curves. For each test that displayed a sawtooth pattern we identified the time instance $\tau^{(\text{slip})}$ at which the sawtooth pattern first started appearing and noted the values of F , w_s , and w_0 at that time instance. We denote those values as $F^{(\text{slip})} := F(\tau^{(\text{slip})})$, $w_s^{(\text{slip})} := w_s(\tau^{(\text{slip})})$, and $w_0^{(\text{slip})} := w_0(\tau^{(\text{slip})})$, and report them in Tables S1 and S2.

Arc length-displacement curves and observation of slip events. In order to investigate the origin of the sawtooth patterns we also constructed $\Delta S-w_s$ curves, which we define as

$$\mathbb{R}_{\geq 0} \ni \tau \mapsto \tau^{\Delta S-w_s} (\Delta S(\tau), w_s(\tau)) \in \mathbb{R}^2, \quad (9)$$

where $\Delta S(\tau) := S(\tau) - L$ is the change in the spicule's arc length from the beginning of the experiment, since at the experiment's beginning the spicule's arc length equals the trench width. The $\Delta S-w_s$ curve from a representative SS failure test that displayed a sawtooth pattern is shown in Fig. 8(D). The $F-w_s$ curve from that test is also shown in Fig. 8(D). We mark the point $(w_s^{(\text{slip})}, F^{(\text{slip})})$ on that curve using a red square, and mark some of the w_s values at which we observe sudden force drops using vertical dashed lines. By comparing the $F-w_s$ and $\Delta S-w_s$ curves in Fig. 8(D), it can be observed that whenever there is a sudden drop in F there is also an abrupt increase in ΔS . That is, for every drop in F there is a corresponding jump in ΔS , and vice versa. We observed this one-to-one correspondence between drops in F and jumps in ΔS in 18 of the 22 SS failure tests whose $F-w_0$ responses displayed the sawtooth pattern.

From tensile tests⁶ on *Ea.* spicules, we know that for the range of stresses that the spicules are exposed to in our bending tests, the spicules are essentially inextensible along their length. Therefore, a jump in ΔS is simply the spicule slipping at the trench edges. In many of the cases, we ascertained the slip event(s) directly by comparing the optical microscopy images of the spicule just before and after a jump in ΔS .

We interpret the observation of the one-to-one correspondence between spicule slip events and force-drop events, as we mentioned previously, by considering the hypotheses (h.1)–(h.3), which, to reiterate, are that (h.1) each force drop is entirely due to a layer-fracture event, of the type that takes place, e.g., during the operation of the Cook-Gordon

mechanism, (h.2) the force drops are due to a combination of layer-fracture and spicule slip event, and (h.3) a force drop is entirely due to its co-slip event(s).

3.1.2. Fixed-fixed set-up

We carried out failure tests in the FF set-up on 12 *Ea.* spicule specimens to investigate the origin of the sawtooth patterns in our SS set-up failure tests. Raw $F-w_0$ curves and scaled $F-w_0$ curves from the FF set-up failure tests are shown in Fig. 7(B) and (D), respectively. For the FF set-up the Euler-Bernoulli theory predicts that the force increases linearly with the displacement as

$$\frac{F(\tau)L^2}{EI} = 192 \frac{w_0(\tau)}{L}. \quad (10)$$

It can be seen from Fig. 7(D) and (10) that when w_0/L is smaller than ≈ 0.005 , the measured $F-w_0$ curves match the one predicted by the Euler-Bernoulli beam theory quite well. As w_0/L continues to increase beyond ≈ 0.005 , some of the $F-w_0$ curves start to become nonlinear, and by the time when $w_0/L \approx 0.02$, most of them have noticeably diverged from the Euler-Bernoulli beam theory's linear prediction.

As can be noted from Fig. 6(D) and 7(B), (D), there are no discernible sawtooth patterns in the $F-w_0$ responses of any of the 12 spicule specimens tested in the FF set-up. From those same figures, it can also be seen that for every spicule tested in the FF set-up, the force F only increases with w_0 —i.e., there are no force drops—until the spicule fails abruptly in a brittle manner. For example, consider the results from a representative FF test shown in Fig. 9. It can be seen from the $F-w_0$ curve shown in Fig. 9(A) that F only increases with w_0 prior to the spicule's complete failure, i.e., there are no force drops in the $F-w_0$ curves that can be considered to be a part of any sawtooth pattern. Some important states during the test, especially around the time when the spicule fails, are shown marked as (1), (2)...(5) on the $F-w_0$ curve. Optical micrographs that show the spicule's deformed configuration in those states are displayed in Fig. 9(C). It can be noted from the zoomed-in view of the $F-w_0$ curve that is shown as an inset Fig. 9(A) that the spicule's failure begins and ends within two stage displacements, and that w_0 changes by less than $4 \mu\text{m}$ during that time. That is, the spicule's failure is quite abrupt, and is quite distinct from the prolonged failure that accompanies the sawtooth patterns observed in the mechanical tests of prototypically tough SBMs.

If the sawtooth patterns in the $F-w_0$ curves from the failure tests conducted in the SS set-up are due to the spicule's fracture behavior, then we would expect to see sawtooth patterns in the $F-w_0$ curves from the failure tests conducted in the FF setup as well. The lack of any sawtooth patterns in the FF tests suggests that the sawtooth patterns in the SS tests are not a characteristic of the spicule's fracture behavior. That is, it supports hypothesis (h.3).

3.2. Load-unload tests

We carried out load-unload tests, which we will describe shortly, for investigating the origin of the sawtooth patterns in the SS failure tests in an alternate manner.

The load-unload tests were similar to the original SS failure tests. However, in contrast to what we did in the original SS failure tests, in these tests we stopped the loading phase before the spicule specimens could fail. Following the loading phase, we unloaded the spicules until the spicules almost regained their straight shape and the force between them and the cantilever's tip was close to zero. As we mentioned in § 2.3, we refer to a pair of consecutive load and unload phases as a load-unload cycle. Each of our load-unload tests involved at least two back to back load-unload cycles.

We carried out six load-unload tests, each of which involved a different spicule specimen. As with the $F-w_0$ curves from the original SS failure tests, some of the $F-w_0$ curves from these tests also displayed

⁶ We plan on describing our tensile tests and presenting the measurements from them, shortly, in a future publication.

sawtooth patterns. The $F-w_0$ curve from a representative load-unload test is shown in Fig. 10(A). The loading and unloading branches are shown using solid and dashed lines, respectively. The curves for different cycles are shown in different colors. In the $F-w_0$ curve shown in Fig. 10(A), if the two force drops visible in the loading phase of the first cycle are due to layer fracture events, then we would expect the slope of the $F-w_0$ curve in the limit $w_0 \rightarrow 0$ in the unloading phase of the first cycle, as well as in the loading and unloading phases of all subsequent cycles, to be smaller than that in the loading phase of the first cycle. This is because the mechanical stiffness of a specimen is necessarily lower when it is damaged than when it is pristine (Ouchterlony, 1981; Bush, 1976), e.g., see the force-displacement response of nacre from *Pinctada margaritifera* that is shown in Fig. 10(C). However, as can be seen in Fig. 10(A), the slopes in the unloading phase of the first cycle as well as in the loading and unloading phases of the second cycle are only negligibly different from that in the loading phase of the first cycle. This observation leads us to conclude that the force-drops in the loading phase of the first cycle are not due to any layer-fracture events.

Thus, in summary, the load-unload tests also support hypothesis (h.3).

4. Concluding remarks

1. Based on the observations that we reported in § 3.1.1, and the investigations of the hypotheses that were motivated by those observations discussed in § 3.1.2 and § 3.2, we have shown that there can be more than one explanation for the sawtooth patterns observed during the flexural testing of SBMs. Therefore, the implication of our study is that sawtooth patterns cannot immediately be taken as a conclusive evidence for the operation of fracture toughness enhancing mechanisms, such as the Cook-Gordon mechanism, especially when the specimen has a slender geometry and is being tested in three-point bending type experiments.
2. Our work, of course, does not mean that sawtooth patterns cannot be genuine manifestations of fracture toughness enhancing mechanisms. Neither does it mean that the spicules other than those from the *Ea*. sponge do not possess any architecture-based fracture toughness enhancing mechanisms.
 - Based on this work and the work of Monn et al., we claim that there is no substantial fracture toughness enhancement in *Ea*. spicules. We also expect there to be no substantial fracture toughness enhancement in spicules that are similar to *Ea*. spicules in their dimensions, function, and numbers per sponge individual.
 - We would not be surprised if the *M. chuni* spicule does indeed display fracture toughness enhancement, as suggested in the work by Levi et al. We say this for two reasons. (i) Based on the results of Monn et al., we expect the Cook-Gordon mechanism to be negated if the layers' curvature is large. In *Ea*. spicules, the (non-dimensional) layer curvature, which we define as the ratio of the layer's thickness to its radius, is ≈ 0.026 . However, in *M. chuni*, the (non-dimensional) curvature is roughly in the range 0.0024–0.01 (Wang et al., 2009, 2011; Levi et al., 1989; Vincent, 2012; Müller et al., 2007). (ii) From an evolutionary perspective, it makes more sense to expect fracture toughness enhancement in *M. chuni* spicules rather than in *Ea*. spicules. This is because the *M. chuni* sponge is anchored to the sea floor by a single spicule, whereas a *Ea*. sponge is anchored to the sea floor by a collection of ≈ 2000 spicules (Weaver et al., 2007). Therefore, a brittle failure event in a *M. chuni* spicule would be catastrophic to the sponge, whereas a similar event in a *Ea*. spicule would be nowhere near as consequential.

Declaration of competing interest

The authors declare that they have no known competing financial interests or personal relationships that could have appeared to influence

the work reported in this paper.

Acknowledgment

We thank Jarod Ferreira and Prof. Pradeep Guduru for their help in constructing the mechanical testing device. The authors gratefully acknowledge support from the National Science Foundation [Mechanics of Materials and Structures Program, grant number 1562656]; H.K. thanks the American Society of Mechanical Engineers and Brown University for the support provided to him through the Haythornthwaite Research Initiation Grant and the Richard B. Salomon Faculty Research Award, respectively; M.A.M acknowledges support from the NASA Rhode Island Space Grant Consortium.

Appendix A. Supplementary data

Supplementary data to this article can be found online at <https://doi.org/10.1016/j.jmbbm.2021.104362>.

Author statement

Wenqiang Fang: Methodology, Formal analysis, Data Curation, Writing – Original Draft, Writing – Review& Editing. **Sayaka Kochiyama:** Validation, Formal analysis, Investigation, Data Curation, Writing – Original Draft, Writing – Review & Editing. **Michael Monn:** Methodology, Software, Formal analysis, Investigation, Data Curation, Writing - Original Draft, Writing – Review & Editing, Project administration. **Haneesh Kesari:** Conceptualization, Methodology, Software, Resources, Writing – Original Draft, Writing – Review & Editing, Supervision, Project administration, Funding acquisition.

References

- Aizenberg, J., Sundar, V.C., Yablon, A.D., Weaver, J.C., Chen, G., 2004. Biological glass fibers: correlation between optical and structural properties. *Proc. Natl. Acad. Sci. Unit. States Am.* 101, 3358–3363.
- Barthelat, F., Rabiei, R., 2011. Toughness amplification in natural composites. *J. Mech. Phys. Solid.* 59, 829–840.
- Barthelat, F., Tang, H., Zavattieri, P., Li, C.-M., Espinosa, H., 2007. On the mechanics of mother-of-pearl: a key feature in the material hierarchical structure. *J. Mech. Phys. Solid.* 55, 306–337.
- Browning, A., Ortiz, C., Boyce, M.C., 2013. Mechanics of composite elasmoid fish scale assemblies and their bioinspired analogues. *J. Mech. Behav. Biomed. Mater.* 19, 75–86.
- Bush, A.J., 1976. Experimentally determined stress-intensity factors for single-edge-crack round bars loaded in bending. *Exp. Mech.* 16, 249–257.
- Clegg, W., Kendall, K., Alford, N.M., Button, T., Birchall, J., 1990. A simple way to make tough ceramics. *Nature* 347, 455–457.
- Cook, J., Gordon, J.E., Evans, C.C., Gordon, J.E., Marsh, D.M., Frank Philip, Bowden, 1964. A mechanism for the control of crack propagation in all-brittle systems. *Proc. Roy. Soc. Lond.* 282, 508–520.
- Currey, J.D., 1977. Mechanical properties of mother of pearl in tension. *Proc. R. Soc. Lond. B Biol.* 196, 443–463.
- W. Deng, H. Kesari, Angle-independent Optimal Adhesion in Plane Peeling of Thin Elastic Films at Large Surface Roughnesses, arXiv preprint arXiv:2004.07459.
- Gere, J.M., 2004. Mechanics of Materials, sixth ed. Brooks/Cole-Thomas Learning, Belmont, CA.
- Jackson, A., Vincent, J.F., Turner, R., 1988. The mechanical design of nacre. *Proc. Roy. Soc. Lond. B* 234, 415–440.
- Kamat, S., Kessler, H., Ballarini, R., Nassirou, M., Heuer, A.H., 2004. Fracture mechanisms of the *strombus gigas* conch shell: ii-micromechanics analyses of multiple cracking and large-scale crack bridging. *Acta Mater.* 52 (8), 2395–2406.
- Kesari, H., Doll, J.C., Pruitt, B.L., Cai, W., Lew, A.J., 2010. Role of surface roughness in hysteresis during adhesive elastic contact. *Phil. Mag. Lett.* 90 (12), 891–902.
- Kolednik, O., Predan, J., Fischer, F.D., Fratzl, P., 2011. Bioinspired design criteria for damage-resistant materials with periodically varying microstructure. *Adv. Funct. Mater.* 21, 3634–3641.
- Levi, C., Barton, J., Guillemet, C., Le Bras, E., Lehude, P., 1989. A remarkably strong natural glassy rod: the anchoring spicule of the *Monorhaphis* sponge. *J. Mater. Sci. Lett.* 8, 337–339.
- Li, X., Chang, W.-C., Chao, Y.J., Wang, R., Chang, M., 2004. Nanoscale structural and mechanical characterization of a natural nanocomposite material: the shell of red abalone. *Nano Lett.* 4, 613–617.
- Mayer, G., 2005. Rigid biological systems as models for synthetic composites. *Science* 310 (5751), 1144–1147.

- Meyers, M.A., Lin, A.Y.-M., Chen, P.-Y., Muyco, J., 2008. Mechanical strength of abalone nacre: role of the soft organic layer. *J. Mech. Behav. Biomed. Mater.* 1, 76–85.
- Ming-Yuan, H., Hutchinson, J.W., 1989. Crack deflection at an interface between dissimilar elastic materials. *Int. J. Solid Struct.* 25 (9), 1053–1067.
- Monn, M.A., Kesari, H., 2017. Enhanced bending failure strain in biological glass fibers due to internal lamellar architecture. *J. Mech. Behav. Biomed. Mater.* 69–75.
- Monn, M.A., Weaver, J.C., Zhang, T., Aizenberg, J., Kesari, H., 2015. New functional insights into the internal architecture of the laminated anchor spicules of *Euplectella aspergillum*. *Proc. Natl. Acad. Sci. Unit. States Am.* 112, 4976–4981.
- Monn, M.A., Ferreira, J., Yang, J., Kesari, H., 2017. A millimeter scale flexural testing system for measuring the mechanical properties of marine sponge spicules. *JoVE*, e56571.
- Monn, M.A., Vijaykumar, K., Kochiyama, S., Kesari, H., 2020. Lamellar architectures in stiff biomaterials may not always be templates for enhancing toughness in composites. *Nat. Commun.* 11, 373.
- Müller, W., Li, J., Schröder, H., Qiao, L., Wang, X., 2007. The unique skeleton of siliceous sponges (porifera; hexactinellida and demospongiae) that evolved first from the urmetazoa during the proterozoic: a review. *Biogeosciences* 4, 219–232.
- Müller, W.E., Wang, X., Kropf, K., Ushijima, H., Geurtsen, W., Eckert, C., Tahir, M.N., Tremel, W., Boreiko, A., Schloßmacher, U., et al., 2008. Bioorganic/inorganic hybrid composition of sponge spicules: matrix of the giant spicules and of the comitalia of the deep sea hexactinellid Monorhaphis. *J. Struct. Biol.* 161, 188–203.
- Munch, E., Launey, M.E., Alsem, D.H., Saiz, E., Tomsia, A.P., Ritchie, R.O., 2008. Tough, bio-inspired hybrid materials. *Science* 322, 1516–1520.
- Osuna-Mascaró, A., Cruz-Bustos, T., Benhamada, S., Guichard, N., Marie, B., Plasseraud, L., Corneillat, M., Alcaraz, G., Checa, A., Marin, F., 2014. The shell organic matrix of the crossed lamellar queen conch shell (*Strombus gigas*). *Comparative Biochemistry and Physiology. Part B. Biochem. Mol. Biol.* 168, 76–85.
- Ouchterlony, F., 1981. Extension of the compliance and stress intensity formulas for the single edge crack round bar in bending. *Fract. Mech. Ceram. Rocks Concr.* 237–256.
- Rabiei, R., Bekah, S., Barthelat, F., 2012. Nacre from mollusk shells: inspiration for high-performance nanocomposites. *Nat. Polym.* 2, 113–149.
- Rahaman, M.M., Fang, W., Fawzi, A.L., Wan, Y., Kesari, H., 2020. An accelerometer-only algorithm for determining the acceleration field of a rigid body, with application in studying the mechanics of mild traumatic brain injury. *J. Mech. Phys. Solid.* 104014.
- Sarikaya, M., Fong, H., Sunderland, N., Flinn, B., Mayer, G., Mescher, A., Gaino, E., 2001. Biomimetic model of a sponge-spicular optical fiber—mechanical properties and structure. *J. Mater. Res.* 16, 1420–1428.
- Smith, B.J., Schaffer, T.E., Viani, M., Thompson, J.B., Frederick, N.A., Kindt, J., Belcher, A., Stucky, G.D., Morse, D.E., Hansma, P.K., 1999. Molecular mechanistic origin of the toughness of natural adhesives, fibres and composites. *Nature* 399, 761.
- Sundar, V.C., Yablon, A.D., Grazul, J.L., Ilan, M., Aizenberg, J., 2003. Fibre-optical features of a glass sponge. *Nature* 424 (6951), 899–900.
- Tamerler, C., Sarikaya, M., 2009. Molecular biomimetics: nanotechnology and bionanotechnology using genetically engineered peptides. *Phil. Trans. Roy. Soc. Lond.* 367 (1894).
- Vincent, J., 2012. *Structural Biomaterials*. Princeton University Press.
- Walter, S., Flinn, B., Mayer, G., 2007. Mechanisms of toughening of a natural rigid composite. *Mater. Sci. Eng. C* 27, 570–574.
- Wang, X., Schröder, H.C., Müller, W.E., 2009. Giant siliceous spicules from the deep-sea glass sponge monorhaphis chuni. *Int. Rev. Cell Mol. Biol.* 273, 69–115.
- Wang, X., Wiens, M., Schröder, H.C., Jochum, K.P., Schloßmacher, U., Götz, H., Duschner, H., Müller, W.E., 2011. Circumferential spicule growth by pericellular silica deposition in the hexactinellid sponge monorhaphis chuni. *J. Exp. Biol.* 214 (12), 2047–2056.
- Weaver, J.C., Aizenberg, J., Fantner, G.E., Kisailus, D., Woesz, A., Allen, P., Fields, K., Porter, M.J., Zok, F.W., Hansma, P.K., Fratzl, P., Morse, D.E., 2007. Hierarchical assembly of the siliceous skeletal lattice of the hexactinellid sponge *Euplectella Aspergillum*. *J. Struct. Biol.* 158, 93–106.
- Wegst, Ulrike G.K., Bai, H., Saiz, E., Tomsia, Antoni P., Ritchie, Robert O., 2014. Bioinspired structural materials. *Nat. Mater.* 14, 23–36.
- Zlotnikov, I., Shilo, D., Dauphin, Y., Blumtritt, H., Werner, P., Zolotoyabko, E., Fratzl, P., 2013. *In situ* elastic modulus measurements of ultrathin protein-rich organic layers in biosilica: towards deeper understanding of superior resistance to fracture of biocomposites. *RSC Adv.* 3, 5798–5802.